A Time-Dependent Multiphysics, Multiphase Modeling Framework for Carbon Nanotube Synthesis Using Chemical Vapor Deposition

Mahmoud Reza Hosseini and Nader Jalili
Smart Structures and Nanoelectromechanical Systems Laboratory, Dept. of Mechanical Engineering, Clemson University, Clemson, SC 29634

David A. Bruce
Dept. of Chemical and Biomolecular Engineering, Clemson University, Clemson, SC 29634

DOI 10.1002/aic.11959
Published online September 25, 2009 in Wiley InterScience (www.interscience.wiley.com).

A time-dependent multiphysics, multiphase model is proposed and fully developed here to describe carbon nanotubes (CNTs) fabrication using chemical vapor deposition (CVD). The fully integrated model accounts for chemical reaction as well as fluid, heat, and mass transport phenomena. The feed components for the CVD process are methane (CH_4), as the primary carbon source, and hydrogen (H_2). Numerous simulations are performed for a wide range of fabrication temperatures (973.15–1273.15 K) as well as different CH_4 (500–1000 sccm) and H_2 (250–750 sccm) flow rates. The effect of temperature, total flow rate, and feed mixture ratio on CNTs growth rate as well as the effect of amorphous carbon formation on the final product are calculated and compared with experimental results. The outcomes from this study provide a fundamental understanding and basis for the design of an efficient CNT fabrication process that is capable of producing a high yield of CNTs, with a minimum amount of amorphous carbon. © 2009 American Institute of Chemical Engineers *AIChE J,* 55: 3152–3167, 2009

Keywords: carbon nanotube, chemical vapor deposition, amorphous carbon, reaction model

Introduction

Carbon nanotubes (CNTs) are one of the most promising class of nanosize materials as evidenced by the attention they have received since their discovery in 1991.[1] CNTs are composed of graphite cylinders, which are often closed at either ends with caps, consisting of pentagonal rings. Geometrically, they can be defined as a honeycomb lattice rolled into a cylinder with hemispherical ends. A wide range of potential applications are considered for CNTs, such as transistors,[2] probes for scanning probe microscopy,[3] high sensitivity microbalances,[4] gas detectors,[5,6] hydrogen storage devices,[7] field emission type displays,[8,9] electrodes in organic light emitting diodes,[10] and nanotweezers for nanoscale manipulation.[11] Each of these applications requires unique CNTs with specific length, diameter, and chirality; however, control of these parameters is considered the main challenge for large scale production methods for CNTs. Furthermore, these processes are not well designed so as to limit the number of CNT defect sites or the production of unwanted byproducts, such as amorphous carbon. Therefore, it is crucial to develop a controlled CNTs fabrication process that is capable of producing pure CNTs with uniform properties.

The goal of synthesizing CNTs in high purity with specified properties requires the development of a detailed and

Correspondence concerning this article should be addressed to N. Jalili at jalili@clemson.edu.

comprehensive CNTs synthesis model that can predict the effect of major processing parameters, such as gas flow rate, the ratio of the feed gas species and synthesis temperature, on the final properties of the CNT products. Constructing a model that can precisely predict the production rate and properties of fabricated CNTs is an impossible task at this time due to the complexity of the required quantum simulations and the large time scale over which reactions occur. However, a detailed, real-time model can provide the insight necessary for the effective production of pure CNTs with uniform properties if it benefits from some in-situ diagnostic systems that provide feedback as to the progression of different reactions within the system.

To study the relations between process temperature, feed gas flow rate, and feed gas molar ratios with CNTs formation, a multiphysics, multiphase model of the CVD system is developed and verified here via comparison to experimental results. The model couples the kinetics of multiple reactions with relevant transport phenomena in such a way that all parameters are solved simultaneously in the time domain.

Overview of CNT Fabrication and Modeling Procedure

Several techniques are available for fabricating CNTs, such as DC torch arc discharge, laser ablation, pulse laser deposition (PLD), sol gel, and chemical vapor deposition (CVD).[12–15] Among these numerous fabrication techniques, the CVD synthesis process has been proven to be a promising method for fabricating CNTs in large quantities because of its simplicity. Therefore, the current CNTs synthesis modeling procedure is based on the CVD fabrication method. Figure 1 depicts the available CVD system in our Smart Structures and Nanoelectromechanical Systems (SSNEMS) Laboratory at Clemson University.[16,17] This system operates at atmospheric pressure and has an upper temperature limit of 1473 K.

In a typical CVD system, methane (CH_4) is used as the gas phase carbon source because of its low cost and stability at high temperatures. Hydrogen (H_2) can also be used to facilitate hydrocarbon reactions that yield CNTs and prevent the decomposition of the methane feedstock into unwanted byproducts. The gaseous species resulting from the decomposition of methane undergo reactions with the catalyst layer, which has been deposited on the silicon wafer to produce carbon molecules and hydrogen as a byproduct. The bulk of the resulting carbon species remain adsorbed on the deposited catalyst nanoparticles atop the silicon substrate. As these nanoparticles become saturated with carbon species, hexagonal carbon rings are formed around the nanoparticles and nanotubes begin to grow on the substrate. Before and after the completion of the CNTs fabrication process, as well as during the heating cycle of the process, argon gas is inserted into the quartz tube in order to reduce the amount of impurities created.

Although the exact formation mechanism of CNTs is not yet known, it has been shown that the CNTs properties are strongly affected by the CVD temperature and inlet gas flow rates used during the fabrication process.[9,18,19] For example, as the synthesis temperature increases, thicker CNTs can be fabricated.[20] To date, there have been several efforts to

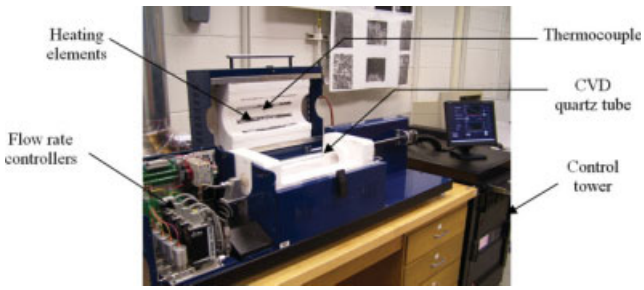

Figure 1. Easytube 1000 CVD (first nano) system at the Clemson University Smart Structures and Nanoelectromechanical Systems (SSNEMS) Laboratory.

[Color figure can be viewed in the online issue, which is available at www.interscience.wiley.com.]

experimentally estimate the carbon growth rate experimentally. However, varied growth rates have been reported, ranging from less than 0.1 to 9 micron/s.[21–27] Geohegan et al. reported that increases in the synthesis temperature lead to an increase in CNT growth rate up to 973 K, where the growth rate starts decreasing.[25] In contrast, other experiments showed similar increases in CNT growth rate with increases in synthesis temperature over the entire range studied.[26] Further, Gunjishima et al. showed that increasing or decreasing the hydrocarbon/hydrogen (C_2H_2/H_2) ratio in the process feed will lead to an increase or decrease, respectively, in the growth rate of CNTs.[28]

In addition to an array of experimental research articles on this topic, there have been a number of published works describing theoretical models of CNT formation and growth. For example, Klinke et al. studied the effect of CVD temperature on CNT diameter and growth rate using a thermodynamic model.[29] Their study showed that as the CVD temperature increases, the deviation between theoretical and experimental growth rate number increases. Grujicic et al. developed a model for a CVD fabrication system[30] by following the work of Coltrin et al.,[31] which described the growth rate of CNTs as a function of temperature for a $CH_4 + H_2$ gas mixture, where the CH_4/H_2 molar ratio was 0.18. Such prior work provides the foundations for the more complete modeling and experimental effort described here.

A finite element method is implemented to model the physical phenomena taking place inside the CVD quartz tube during the CNT fabrication process. In the considered CVD model, a range of CH_4 and H_2 gas flow rates were examined in order to investigate the effects of vapor phase composition on the quality and growth rate of CNTs. The CH_4 flow rate was varied from 500 to 1000 sccm, while the flow rate of H_2 ranged from 250 to 750 sccm as a part of inlet boundary condition. A schematic of the modeled CVD system and the considered grid distribution along CVD quartz tube is shown in Figure 2.

The quartz tube is considered to be 30 cm in length and have an inside diameter of 5.5 cm. This is based on the dimensions of the available CVD system in SSNEMS Laboratory. The modeled silicon substrate is 6 cm long and is centrally located within the simulated quartz tube. It is assumed that a catalyst layer containing well dispersed

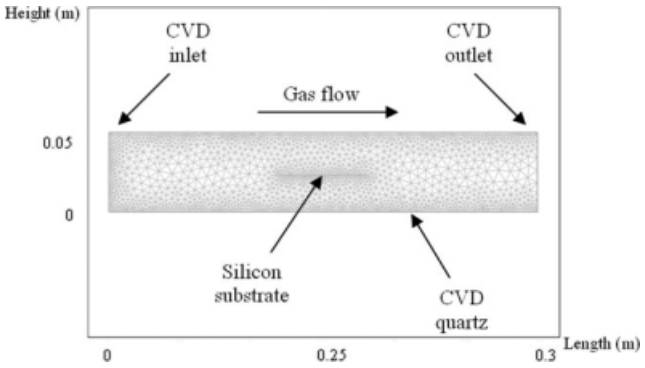

Figure 2. Schematic of modeled CVD system and finite element grid distribution used in modeling the quartz tube reactor assembly.

nanoparticles is deposited on the silicon. Cobalt (Co) nanoparticles are used as catalyst because they have been shown to be highly active and selective at forming CNTs under the processing conditions of interest.[32,33] The triangle meshing system was utilized, and the size of the elements were refined at the inlet and quartz tube wall boundaries, as well as around the substrate, where reactions and sudden changes in flow properties take place and the complexity of calculations increases dramatically.

The simulated pressure is considered to be equal to atmospheric pressure condition in order to meet with our CVD system specifications. Because the reaction rate as well as the physical and flow properties of the reactant gases are temperature dependent, we have extended our studies to investigate temperature effects on growing CNTs during the fabrication process. Therefore, the temperature is varied from 973.15 to 1273.15 K and are imposed as the wall boundary condition during each simulation. During the simulations, instead of considering an average value, the physical and transport properties of each species are calculated at the conditions present at each node of the finite element mesh in order to further improve the accuracy of the present modeling investigations. The carbon species participating in CNTs construction are created by collision induced reactions occurring in the gas phase as well as surface catalyzed reactions on the substrate. Specific details about the modeling procedures used to simulate the gas phase and surface reactions are discussed in the following sections.

Mathematical and Modeling Procedure

The developed multiphysics, multiphase CVD model accounts for gas and surface phase reactions as well as fluid, heat, and mass transport phenomena. A schematic diagram of the mathematical modeling procedure illustrating the interactions between these modules is depicted in Figure 3. As seen, the initial and boundary conditions are inserted into a multiphysics solver to estimate CNT growth rate as well as changes in the physical properties of the reacting species at a range of positions inside the quartz tube.

During the heating phase of the process model, it is assumed that argon gas is inserted into the system and that no reaction takes place in the gas phase or on the substrate surface. As the $CH_4 + H_2$ feed gases enter the modeled quartz tube, the boundary conditions and appropriate species property information are inserted into the mass transport, heat transfer, and fluid mechanics modules to calculate updated physical properties for each species present. Later, the concentration and thermodynamic state properties of all species at a given node are transferred to the gas phase reaction calculator, where reaction rates and the concentration of all species created or consumed by gas phase reactions are calculated. The updated gas phase concentration data are then sent to the transport module in order to recalculate the physical properties of all species.

In the next step, the concentration and physical property information of gas phase species are transferred to the surface phase reaction module, where surface catalyzed reaction rates and the concentrations of adsorbed species are calculated. These values are then sent to the transport solvers as well as the synthesized carbon molecule analyzer so as to quantize the local amount and growth rate of CNTs and amorphous carbon species. The coupled equations are solved numerically considering a fixed time and by applying the aforementioned algorithm until convergence is achieved. In

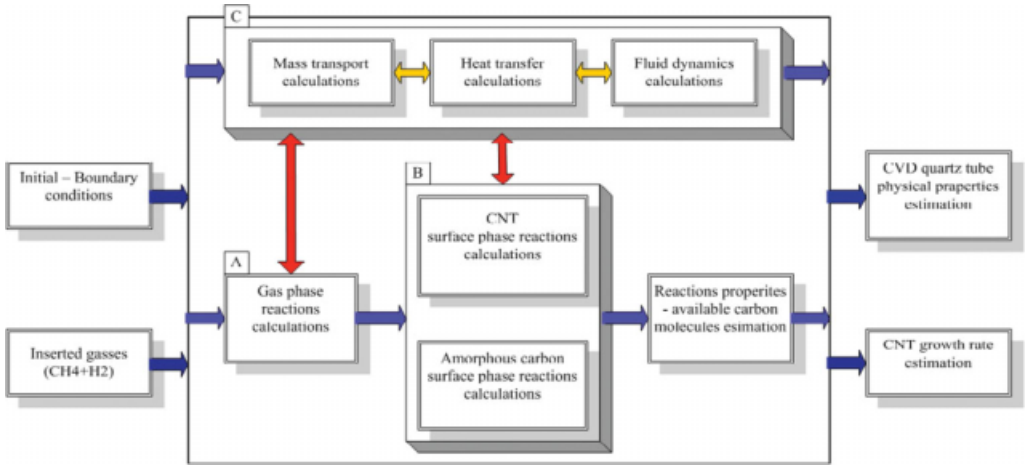

Figure 3. Schematic diagram of mathematical modeling procedure.

[Color figure can be viewed in the online issue, which is available at www.interscience.wiley.com.]

the next step, the simulation is progressed in time and by considering a 10^{-4} second time step size. This simulation procedure is performed until steady-state reaches and the transitional physical properties transform into either a constant value or constant rate of change. Finally, all of the calculated data are combined to predict overall CNT growth rates and the range of physical and species properties with respect to time, observed within the modeled quartz tube, shown in Figure 3. Each of the simulation modules described above is discussed in greater detail below.

Gas phase reaction modeling (Block A in Figure 3)

Gas phase reactions are introduced as a part of major Block A, which models the thermal decomposition of gases inside the CVD quartz tube. Most available models suggested for the decomposition of methane were primarily developed for combustion processes that exhibit high levels of hydroxide gases.[31,34–36] Moreover, the model developed by Coltrin et al. is based on a plasma-gun reactor system, where hydrogen dissociates inside the plasma-gun, thereby, making it unsuitable for our reaction system, which is not a plasma-gun CVD reactor system.[31] Along this line of reasoning, we propose a new set of gas phase reactions for $CH_4 + H_2$ decomposition. The developed model consists of 60 reversible reactions as listed in Table A1 in Appendix A. It is considered that CH_4 and H_2 are the feed gases to the CVD quartz tube. These species are then allowed to undergo thermal decomposition reactions, which creates 11 different new species (CH_3, CH_2, CH, C, C_2H, C_2H_2, C_2H_3, C_2H_4, C_2H_5, C_2H_6, and H). These species then participate in a restricted set of catalyzed surface phase reactions on the substrate.

In the proposed model, the hydrocarbons of radical fragments larger than C_2 are neglected as Coltrin et al. suggests as they can lead to errors in the prediction of the gas phase composition.[31] The reaction rates can be described by the mass action law.

$$r_j = -k_{\mathrm{f}_j} \prod_i c_i^{\nu_{ij}^{\mathrm{r}}} + k_{\mathrm{r}_j} \prod_i c_i^{\nu_{ij}^{\mathrm{p}}} \tag{1}$$

where k_{f_j} and k_{r_j} represent forward and reverse rate constants, c_i denotes the concentration of the ith species (mol/m^3), ν_{ij}^{r} and ν_{ij}^{p} are stoichiometric coefficients of reactants and products, respectively. The material balance for species i can be expressed as:

$$\frac{\partial c_i}{\partial t} + \nabla N_i = r_i \tag{2}$$

where N_i is the molar flux, c_i is the concentration and r_i is the reaction rate of the ith species. It is also assumed that the temperature dependence for all reaction rates can be described by the modified Arrhenius law model:

$$k_{f,i} = A_i T^{n_i} \exp\left(-\frac{E_i}{RT}\right) \tag{3}$$

where A_i represents the frequency factor, T is the reaction temperature, n_i is the temperature factor, E_i denotes the activation energy, and R is the universal gas constant. All reverse reaction rates are calculated using equilibrium thermodynamic models:

$$k_{r,i} = \frac{k_{\mathrm{f},i}}{K_i^{\mathrm{eq}}} \tag{4}$$

where K_i^{eq} denotes an equilibrium constant, which is defined as follow:

$$K_i^{\mathrm{eq}} = \exp\left(-\frac{\Delta G_i}{RT}\right) \tag{5}$$

where ΔG_i is the Gibbs free energy for reaction, which is defined as:

$$\Delta G_i = \Delta H_i - T\Delta S_i \tag{6}$$

In the above expression, ΔH_i and ΔS_i denote the enthalpic and entropic changes in system energy, respectively. These changes occur as a result of chemical reactions and can be calculated using temperature-dependent NASA polynomial relations, which are discussed later in the text. These quantities are calculated for each species. The position specific species concentration data obtained from the gas phase reaction model are inputs to the surface phase reaction model described below.

Surface phase reaction modeling (Block B in Figure 3)

The thermal decomposition of feed gases, the reactive free radical intermediates CH_3, C_2H_2, and H initiate a series of surface reactions with the catalyst layer that has been deposited on the silicon substrate. These surface reactions lead to the production of macromolecular carbon species in the form of CNTs or amorphous carbon. Following the work of Grujicic et al.,[30] the surface reaction model uses two sets of surface reactions that result in the deposition of CNTs or amorphous carbon.

For the production of CNTs, 19 reversible surface reactions are considered that lead to the creation of 11 new surface species (TH(S), TCH_3(S), TCH_2(S, R), TCH(S, R_2), TC(S, R_3), TC_2H_2(S), TC_2H(S, R), TC_2(S, R_2), TCH_2CH_3(S), $TCHCH_3$(S, R), and $TCCH_3$(S, R_2)). The surface reactions leading to the deposition of CNTs are depicted in Table A2 in Appendix A. In this table, T(S) denotes the deposited cobalt nanoparticles on the substrate surface, and symbols G, S, and B represent gas phase, surface phase, and carbon nanotube bulk species, respectively. Also, R, R_2, and R_3 denote species that are single, double, or triple radicals, respectively.

In the surface phase reaction model, reactions with H lead to the passivation of the substrate nanoparticles. However, reactions with CH_3 and C_2H_2 give rise to chemisorption of hydrocarbon molecules on the substrate surface. Surface species TC(S, R_3) and TC_2(S, R_2), which participate the CNTs synthesis, are formed by hydrogen abstraction from hydrocarbons and hydrocarbon radicals. Similar to the gas phase reactions, surface phase reactions obey the mass action law, with the forward reaction constants calculated using a modified Arrhenius relation (see Eq. 3). The list of Arrhenius parameters for each forward reaction is shown in Table A2.

Also, reverse reaction rate constants were calculated by Eq. 4 using the appropriate equilibrium reaction constant.

The surface reactions that lead to the formation of amorphous carbon involve eleven surface species (C(S,R), C(S,R_3), CH(S), CH(S,R), CH(S, R_2), CH_2(S, R), CH_2(S), CH_2(S, R), CH_3(S), C_2H_2(S, R), C_2H_3(S)) and a bulk species C(A), which are listed in Table A3. Similar to the surface reactions leading to CNTs formation, these reactions occur on catalytic sites that contain the H, CH_3, and C_2H_2 active intermediates, which are all products of previously described gas phase reactions.

Many of the surface reactions listed in Table A3 obey the reaction probability law. For example, when gas phase species react with surface species via an Eley-Rideal type mechanism (A(G)+B(S) $\rightarrow$ product), the reaction probability upon the collision of A(G) and B(S) is defined by γ:

$$\gamma_i = a_i \exp\left(\frac{-b_i}{RT}\right) \tag{7}$$

where a_i is a unit less parameter and b_i has units of energy that are compatible with the universal gas constant R. Because the value of γ_i defines the probability, its value lies between 0 and 1. By applying probability γ_i, it is possible to express the mass-action kinetic rate constant as:

$$k_{f,i} = \left(\frac{\gamma_i}{1-(\gamma_i/2)}\right)\frac{1}{\Gamma^m}\left(\frac{RT}{2\pi W}\right)^{1/2} \tag{8}$$

where W is the molecular weight of the gas phase species, Γ is the total surface-site density, and m is the sum of all of the stoichiometric coefficient for the surface reactants. The term Γ raised to the power m accounts for converting unit less reaction probabilities to units suitable for the reaction rate constant, and the square root arises from the gas phase collision frequency.

The conversion between the surface reaction rate of production of a bulk species $\dot{s}_k$ (mol/cm^2/s) and a growth rate R_{NT} (cm/s) can be defined as

$$R_{NT} = \frac{\dot{s}_k W_k}{\rho_k} \tag{9}$$

In the above equation, ρ_k is the density of the bulk species redefined as:

$$\rho_k = \frac{m_k}{A_k l_k} \tag{10}$$

where m_k is the mass, A_k is the surface area and l_k is the height of the deposited species.

For both CNTs and amorphous carbon species, the rate at which carbon is transferred from the gas phase is expressed as the number of carbon atoms per unit time. Therefore, the product of the carbon deposition rate and the number of carbon deposition sites on the particle surface (number of C atoms per minute per deposit) should equal to the CNTs growth rate and the number of nanotube edge sites (number of C atoms per minute per edge site). Thus, it is possible to define a ratio between CNTs growth rate and the carbon deposition rate for the given particle size and shape. For these calculations, it is assumed that the particles are semi-spherical with a radius equal to that of the respective CNTs.

Fluid dynamics modeling (Block C in Figure 3)

The governing equation for fluid dynamics is based on the Navier-Stokes equation, which can be defined in the following general form.

$$\rho\left(\frac{\partial v}{\partial t} + v\cdot\nabla v\right) = -\nabla P + \mu\nabla^2 v + f \tag{11}$$

where ρ and μ, respectively, stand for density and viscosity, v is the velocity profile of the inserted gas, P is the system pressure, t is time, and f denotes any possible external force. If the gases are considered to be Newtonian and the system density is constant with time, this equation can be expanded for flow in x and y directions to yield:

$$\rho\left(\frac{\partial u}{\partial t} + u\frac{\partial u}{\partial x} + v\frac{\partial u}{\partial y}\right) = -\frac{\partial P}{\partial x} + \mu\left(\frac{\partial^2 u}{\partial x^2} + \frac{\partial^2 u}{\partial y^2}\right) + f_x \tag{12}$$

$$\rho\left(\frac{\partial v}{\partial t} + u\frac{\partial v}{\partial x} + v\frac{\partial v}{\partial y}\right) = -\frac{\partial P}{\partial y} + \mu\left(\frac{\partial^2 v}{\partial x^2} + \frac{\partial^2 v}{\partial y^2}\right) + f_y \tag{13}$$

At each node of the model, the Navier Stokes equations are coupled with continuity equation as:

$$\frac{\partial \rho}{\partial t} + (\nabla\cdot\rho v) = 0 \tag{14}$$

To calculate mass flow rate from volumetric flow rate information as the inlet boundary condition, the ideal gas law is combined with a simple density-mass relation:

$$\dot{m} = \frac{mP}{nRT}(vA) \tag{15}$$

where $\dot{m}$ represents mass flow rate, m is the mass of one mole of inserted gas species, v is the gas velocity, A is the quartz tube cross-sectional area, P is the system pressure, and T and V are the temperature and volume of the system, respectively.

Given the low system pressure, the ideal gas law can also be used to calculate the fluid density in the following form:

$$\rho = \frac{P}{RT}\sum_i x_i M_i \tag{16}$$

where x_i and M_i denote the mole fraction and molar weight of the ith species, respectively.

For this model, nonslip boundary conditions are assumed near the quartz tube wall as well as on the substrate surface. This assumption is valid based on the system pressure and the fact that the surfaces are known to contain a thin layer of stationary adsorbed molecules.

Mass transport modeling (Block C in Figure 3)

To effectively model mass transport and surface diffusion phenomena, the following mass balance equation is used:

$$\frac{\partial c_i}{\partial t} + \nabla \cdot (-D_i \nabla c_i + c_i v) = r_i \tag{17}$$

As defined earlier, c_i and r_i are concentration and reaction rate of the ith species, respectively, and D_i is the diffusion coefficient for component i in the mixture. Considering the diffusion between each of the two species (species A and B), it is possible to estimate an approximate value for the diffusivity using the binary diffusion coefficients D_{AB}, which are calculated using the following expression derived from kinetic gas theory:

$$D_{AB} = 2.695 \times 10^{-3} \frac{\sqrt{T^3 (M_A + M_B)/(2 \times 10^3 M_A M_B)}}{p \sigma_A \sigma_B \Omega_D} \tag{18}$$

In the above equation, σ_A and σ_B represents the distance in the Lennard-Jones potential at which the interparticle potential is zero, M_A and M_B are the mass of each species, and Ω_D denotes the collision integral, which is given by[37,38]:

$$\Omega_D = A(T^*)^{-B} + C[\exp(-DT^*)] + E[\exp(-FT^*)] + G[\exp(-HT)] + \frac{0.19\delta_{AB}^2}{T^*} \tag{19}$$

where

$$T^* = k\frac{T}{\varepsilon_{AB}} \tag{20}$$

$$\varepsilon_{AB} = (\varepsilon_A \varepsilon_B)^{1/2} \tag{21}$$

$$\delta_{AB} = (\delta_A \delta_B)^{1/2} \tag{22}$$

$$\delta = \frac{1}{2}\frac{\eta^2}{\varepsilon \sigma^3} \tag{23}$$

In the above relations, ε is the activation energy and η denotes the molecular dipole moment (Debye). Also, the following relation is used to calculate dynamic viscosity[37,38]:

$$\mu_i = 2.669 \times 10^{-6} \frac{\sqrt{T(M_i \times 10^3)}}{\sigma_1^2 \Omega_v} \tag{24}$$

where Ω_v is the collision integral and is calculated using the expression:

$$\Omega_v = A(T^*)^{-B} + C[\exp(-DT^*)] + E[\exp(-FT^*)] + \frac{0.20\delta_{AB}^2}{T^*} \tag{25}$$

Thermal and heat transfer modeling (Block C in Figure 3)

Heat transfer by conduction, convection, and radiation are all considered in the current modeling. The following general form of the energy balance is used:

$$\rho C_p \frac{\partial T}{\partial t} + \nabla \cdot \left(-k\nabla T + \rho C_p T v\right) = Q \tag{26}$$

where C_p and k are heat capacity and thermal conductivity of each species, respectively, Q is an ever-present heat source that maybe introduced into the system, and v and T are the respective velocity and temperature related to each node. Through the CVD process, radiation from the heating coils is capable of transferring considerable amounts of energy into the substrate. Therefore, it is necessary to consider this radiative heat transfer process in the model in the following form:

$$Q = \varepsilon_s \sigma_B \left(T_t^4 - T^4\right) \tag{27}$$

where ε_s is the surface emissvity, σ_B denotes the Stefan-Boltzmann constant, and T_t is the quartz tube temperature.

The enthalpy or heat of reaction (H_j) can be calculated from species properties and the stoichiometric coefficients (v_{ij}) in the following form:

$$H_j = -\sum_i v_{ij} h_i \tag{28}$$

Similarly, the entropy of reaction is calculated based on the following expression,

$$S_j = -\sum_i v_{ij} s_i \tag{29}$$

In the above equations, h_i and s_i are the species molar enthalpy (J/mol) and entropy (J/(mol K)) at the specified node temperature, respectively. Applying the above equation, the thermal heat source due to the reaction (J/m^3 s) can be calculated as:

$$Q = V \sum_j H_j r_j \tag{30}$$

where V is the system volume.

Thermal properties, such as species heat capacity $C_{p,i}$, molar enthalpy h_i, and molar entropy s_i of each species, are calculated based on NASA polynomials as:

$$C_{p,i} = R(a_1 + a_2 T + a_3 T^2 + a_4 T^3 + a_5 T^4) \tag{31}$$

$$h_i = R(a_1 + \frac{a_2}{2}T^2 + \frac{a_3}{3}T^3 + \frac{a_4}{4}T^4 + a_5 T^5 + a_6) \tag{32}$$

$$S_i = R(a_1 \ln T + a_2 T + \frac{a_3}{2}T^2 + \frac{a_4}{3}T^3 + \frac{a_5}{4}T^4 + a_7) \tag{33}$$

where $a_1 - a_7$ are NASA polynomial constants. Finally, the thermal conductivity of each gas species can be expressed by the Sticl-Thodos equation[39]:

$$k_i = \frac{\mu_i}{M_i}(1.15C_p + 0.88R) \tag{34}$$

The developed physical solvers were fully coupled and applied to the constructed finite element domain to investigate the CNT and amorphous carbon growth rate. The obtained results are discussed in the following section.

Numerical Results and Discussions

Applying the constructed multiphysics-multiphase model, numerous simulations are conducted to investigate gas flow rate and temperature effects on CNTs growth rate. During each simulation, both inserted gas ratio (CH_4/H_2 in the inlet gas feed) and temperature are considered to be constant and the amount of production of each gas or surface species is calculated. The species production rates resulting from gas or surface phase reactions are shown in Figures 4–8.

By examining the resulting concentrations of gas (CH_3, C_2H_2, H) and surface phase species (C(B) and 2C(B)) for the specified inlet gas mixtures, depicted in Figures 4–8, it can be observed that increases in the fabrication temperature lead to higher amounts of each of these species being produced. Therefore, higher reaction temperatures increase the number of carbon intermediates that participate in CNTs formation. The results also suggest that these increases in intermediate species concentrations lead to increases in the length, diameter of CNTs and may also lead to an increase in CNTs growth rate or the number of CNT's wall layers.

Analysis of gas phase reaction products indicates that increases in the amount of inserted H_2 gas significantly increases the production rate of the H intermediate. Also, increasing the flow rate of CH_4 into the reaction chamber yields only moderate increases in the gas phase H concentration. For the other two species (CH_3 and C_2H_2), any increase in the flow rate of hydrocarbon gas raises CH_3 and C_2H_2 concentrations considerably. However, unlike the behavior observed for H species, increasing the inlet flow of hydrogen decreases the rate of production of CH_3 and C_2H_2 species. One possible cause for this phenomenon is simply the fact that increasing the inlet flow of hydrogen causes a decrease in the mass fraction of hydrocarbon gas in the inlet gas mixture combination.

Investigation of the surface reaction species reveals that C and 2C species respond differently to changes in H_2 and CH_4 gas flow rates. The C concentration data shown in Figure 7 demonstrate that increasing the amount of H_2 gives rise to an increased C production rate. In contrast, any increase in the amount of hydrocarbon gas will decrease the C production rate. On the other hand, inserting more CH_4 gas into the system promotes increased 2C production. This phenomenon is especially evident at lower flow rates of hydrogen (250 sccm). Also, from these diagrams it can be concluded that unlike C, increasing the amount of hydrogen in the inlet gas mixture will reduce the amount of 2C. An explanation for such a phenomenon can possibly be explained by considering the C—C (331.3 kJ/mol) and C—H (415.8 kJ/mol) bond energy values. Because the C—C bond energy is lower, it suggests that the activation energy required to form that bond is lower, which means that the rate of formation of C—C bond types should be higher. This can also be considered as one of the reasons for considerably higher TC_2 production rates as compared to TC species for any particular temperature and inlet gas mixture flow rate that produces bulk carbons.

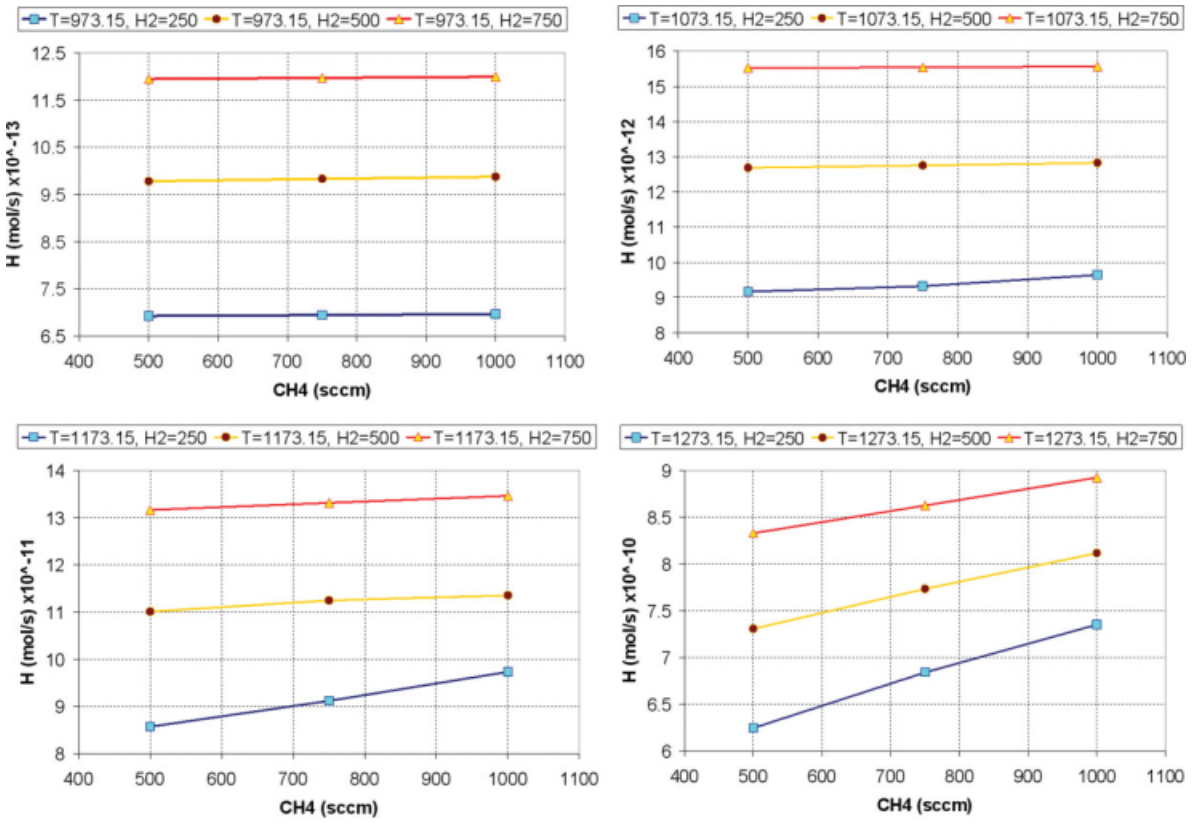

Figure 4. Production rate of H for different CH_4 + H_2 flow rates (sccm) and temperatures (K) (gas phase).

[Color figure can be viewed in the online issue, which is available at www.interscience.wiley.com.]

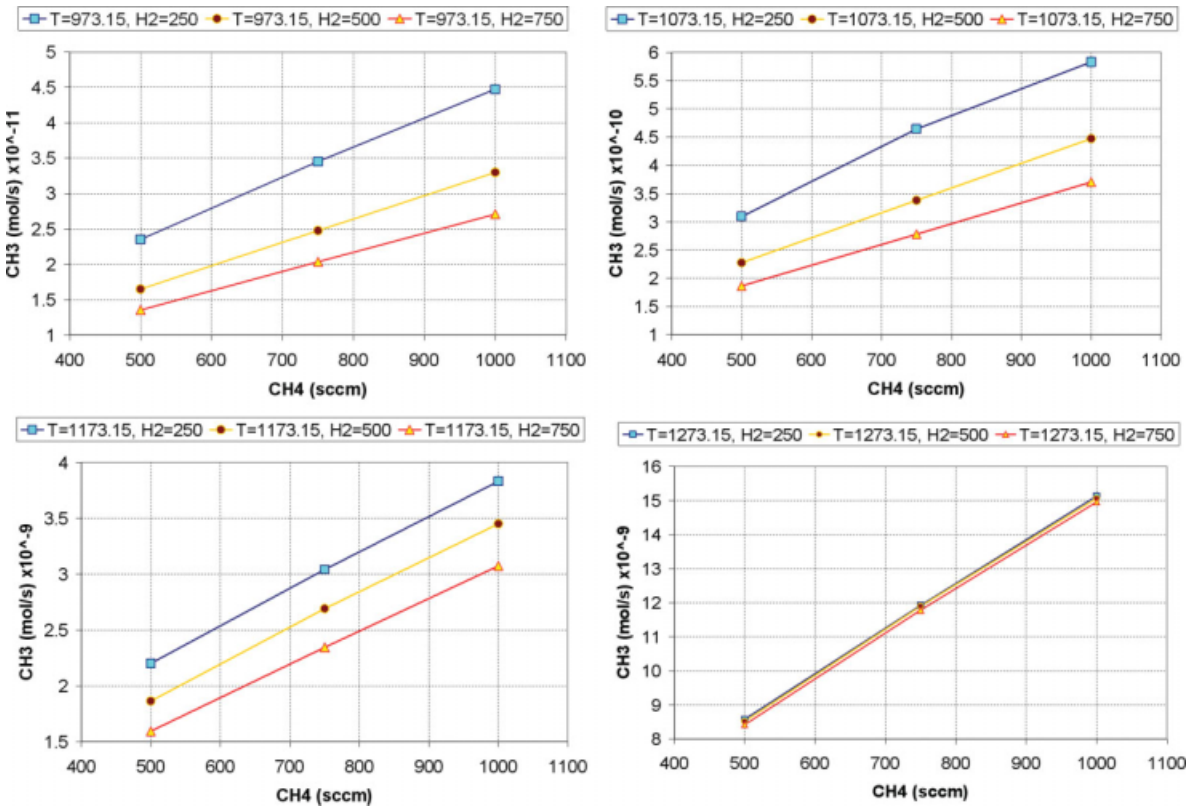

Figure 5. Production rate of CH_3 for different CH_4 + H_2 flow rates (sccm) and temperatures (K) (gas phase).

[Color figure can be viewed in the online issue, which is available at www.interscience.wiley.com.]

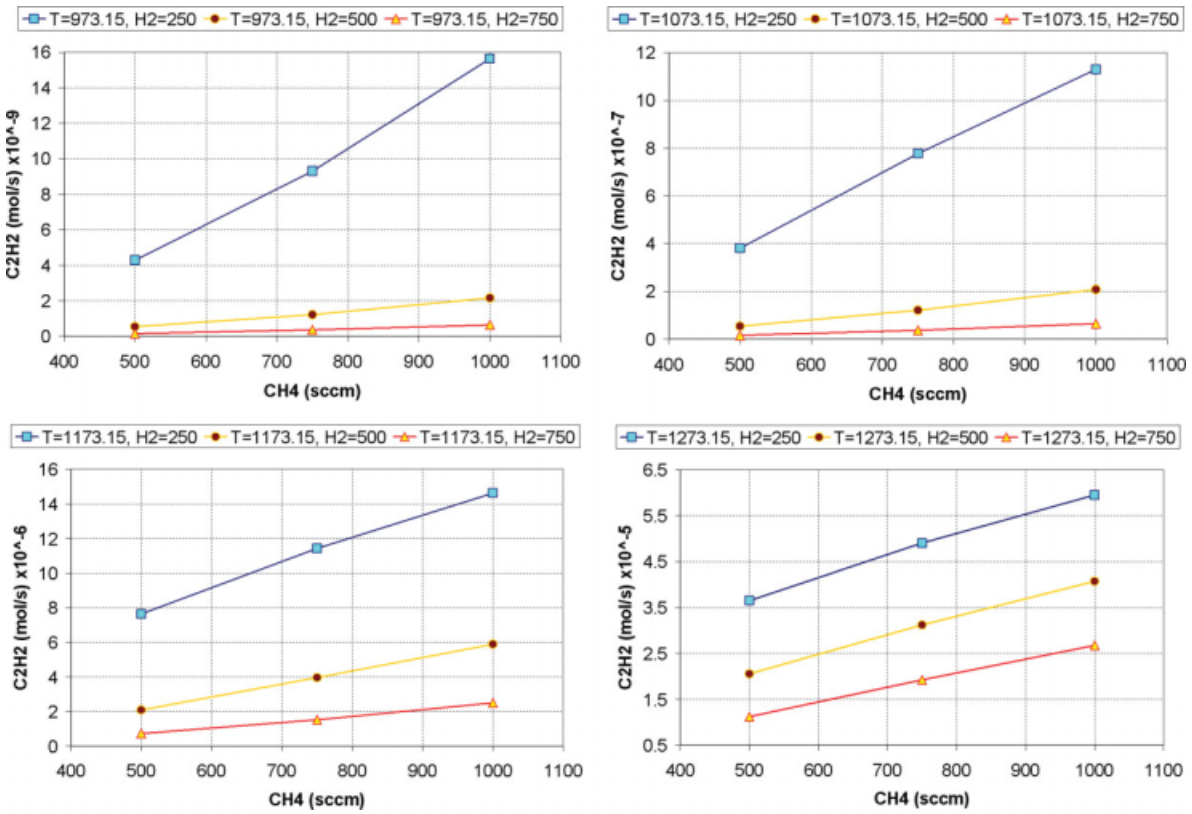

Figure 6. Production rate of C_2H_2 for different CH_4 + H_2 flow rates (sccm) and temperatures (K) (gas phase).

[Color figure can be viewed in the online issue, which is available at www.interscience.wiley.com.]

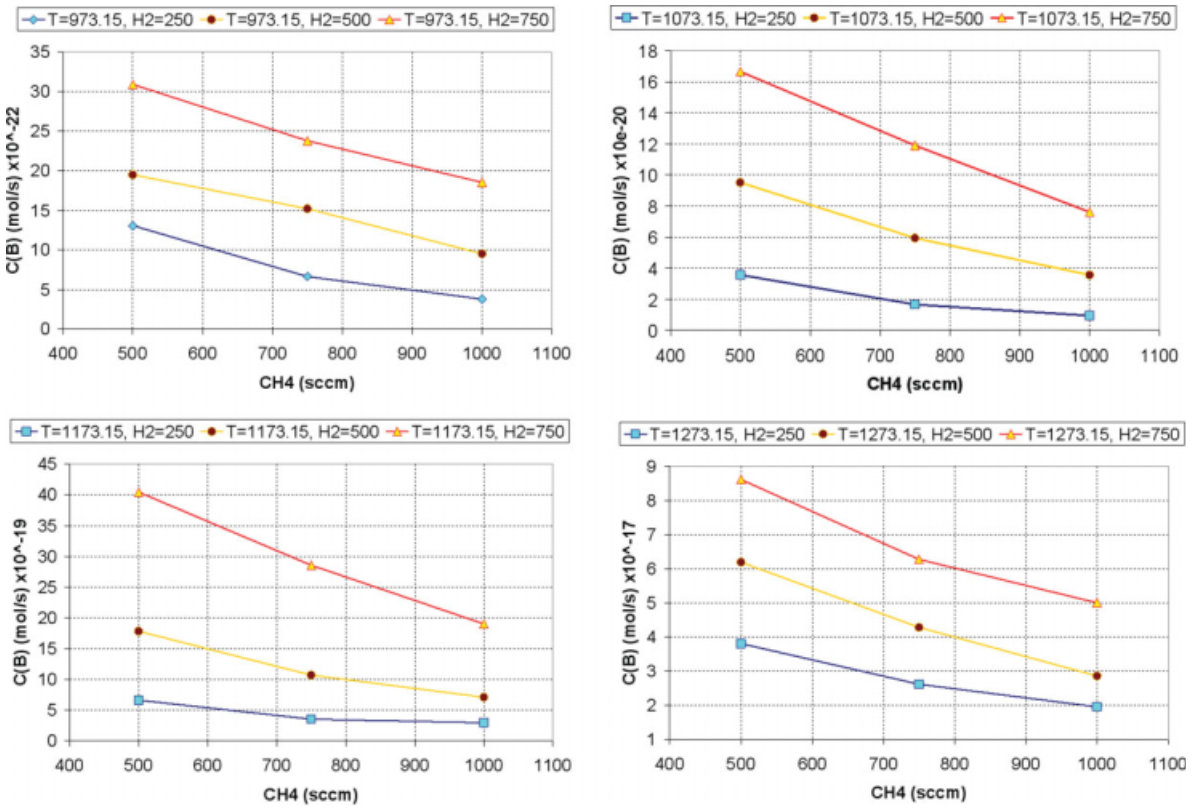

Figure 7. Production rate of C(B) for different CH_4 + H_2 flow rates (sccm) and temperatures (K) (surface phase).

[Color figure can be viewed in the online issue, which is available at www.interscience.wiley.com.]

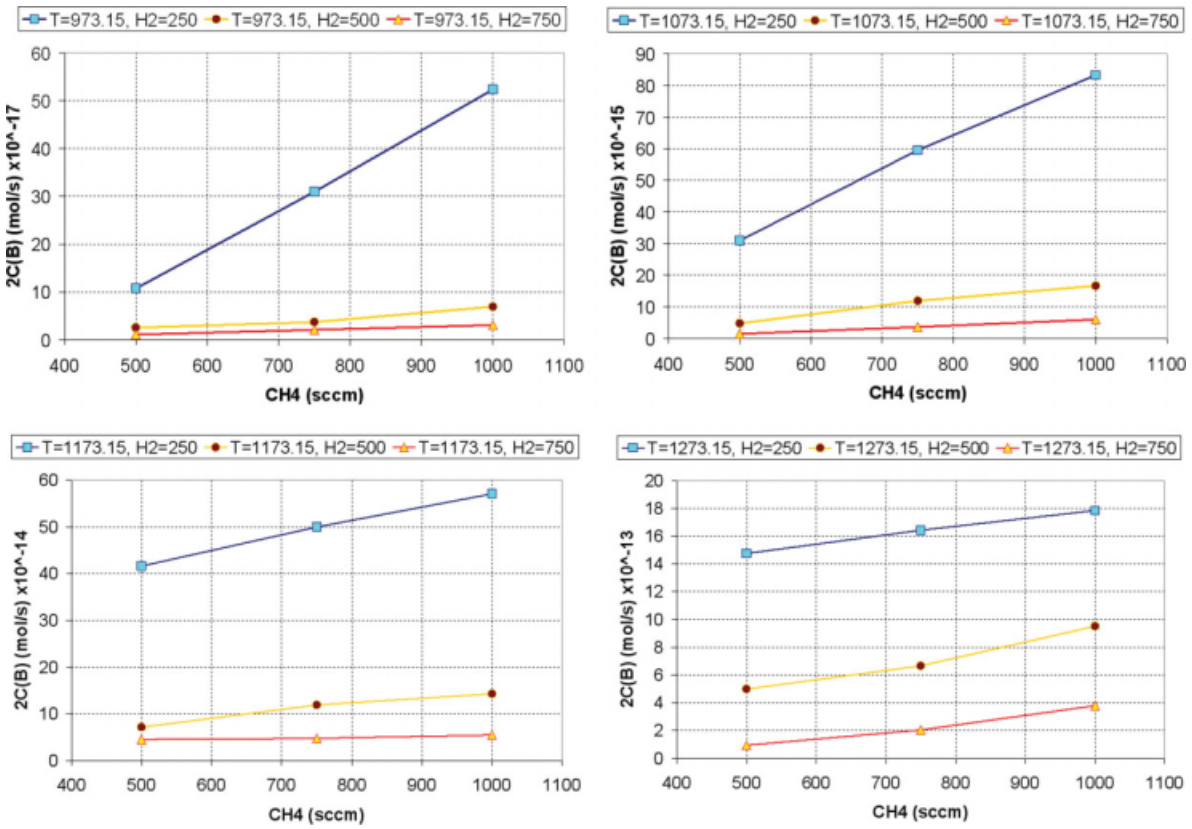

Figure 8. Production rate of 2C(B) for different CH_4 + H_2 flow rates (sccm) and temperature (K) (surface phase).

[Color figure can be viewed in the online issue, which is available at www.interscience.wiley.com.]

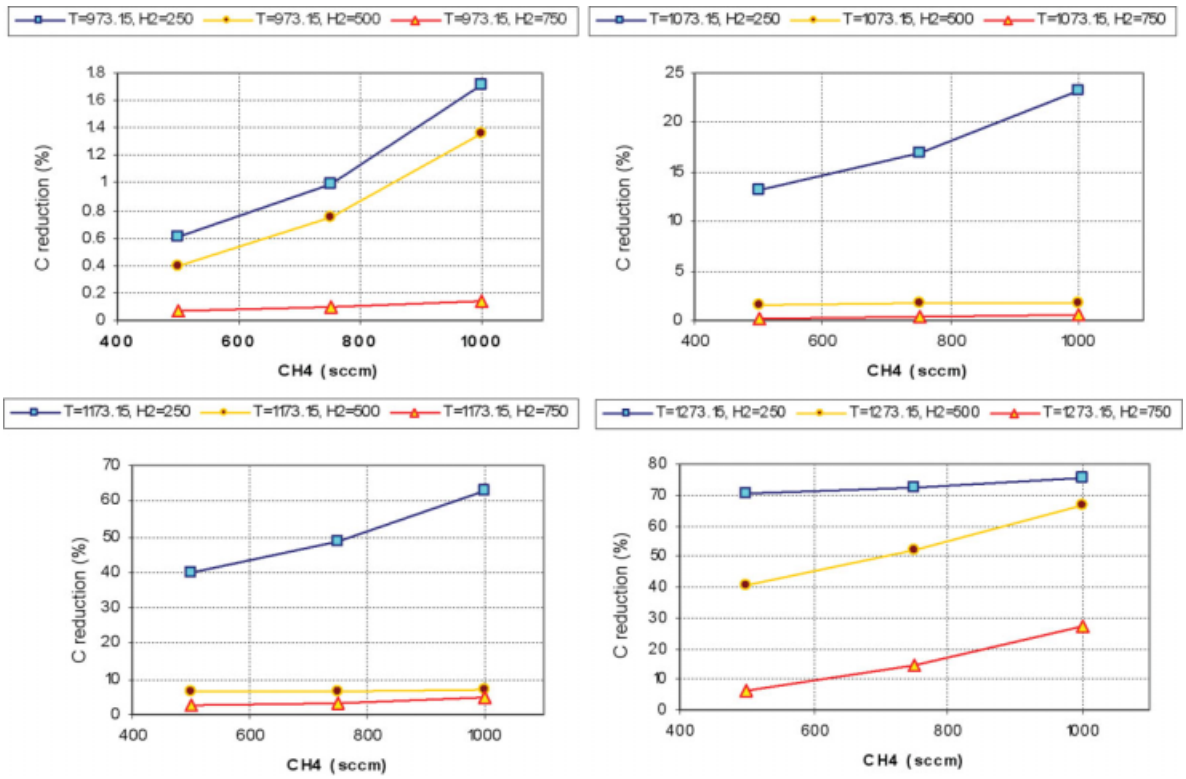

Figure 9. The percentage of carbon decay that participates in CNT construction for different CH_4 + H_2 flow rates (sccm) and temperatures (K).

[Color figure can be viewed in the online issue, which is available at www.interscience.wiley.com.]

Increasing the amount of the hydrogen gas will increase the number of moles of hydrogen and promote the probability of C—H bond formation. Consequently, any rise in hydrogen gas will result in higher TC and lower TC_2 production.

The produced carbon molecules can form either CNTs on the substrate or amorphous carbon, which would be considered as an unwanted byproduct. The created amorphous carbon can be deposited on top of the catalyst layer and interrupts CNTs growth or even preventing any CNTs ring formation around the catalyst nanoparticles. Moreover, producing a high yield of CNTs with the minimum amount of unwanted byproducts is another important matter in the industrial scale production of CNTs. Therefore, it is essential to include amorphous carbon formation reactions into the developed CVD-based CNTs fabrication model to investigate the effects of inserted gas flow rate ratios and synthesis temperature on the formation of amorphous carbon.

Including Table A-3 (see Appendix A) in our surface phase reaction sets, we were able to estimate the amount of reduction in the production grate of carbon molecules that participate in CNTs formation due to the introduction of amorphous carbon under different CNTs fabrication conditions. The obtained results are depicted in Figures 9 and 10.

Figures 9 and 10 show that the percentage of carbon decay (similarly the rate of amorphous carbon production) is less at lower synthesis temperature ranges. However, as the temperature increases, this percentage will increase dramatically especially in the 1173–1273 K range, where it reaches values higher than 70%. Also, it can be seen that at every temperature studied, raising the amount of inserted hydrocarbon gas will lead to an increase in the production percentage of amorphous carbon. Observing the trends in Figures 9 and 10, it is also possible to investigate the role of H_2 in the process of carbon reduction and amorphous carbon formation. It is observed that introducing H_2 in the fabrication process will increase the overall fraction of carbon molecules that participate in the formation of CNTs structure by reducing the amorphous carbon production rate. This percentage of overall increase is more pronounced at higher temperatures.

Also, from the diagrams in Figure 10 it is observed that at low process temperatures, variation in H_2 flow rate have only moderate impact on the amount of amorphous carbon produced, which is in contrast to the trend observed at high temperatures. This suggests that applying H_2, especially at high fabrication temperatures, will lead to a cleaner final product with less amorphous carbon. At lower temperatures, hydrogen is less effective because the overall amount of CNTs which have been produced via gas phase reactions is considerably lower when compared with the amount observed at high fabrication temperatures. It should be mentioned that the rate of production of amorphous carbon is proportional to the reduction in the rate of formation of carbon species that are involved in the production of CNTs. Therefore, as the percentage of carbon decay that participates in CNTs construction increases, it can be expected that less amorphous carbon will form on both the substrate surface and quartz tube wall.

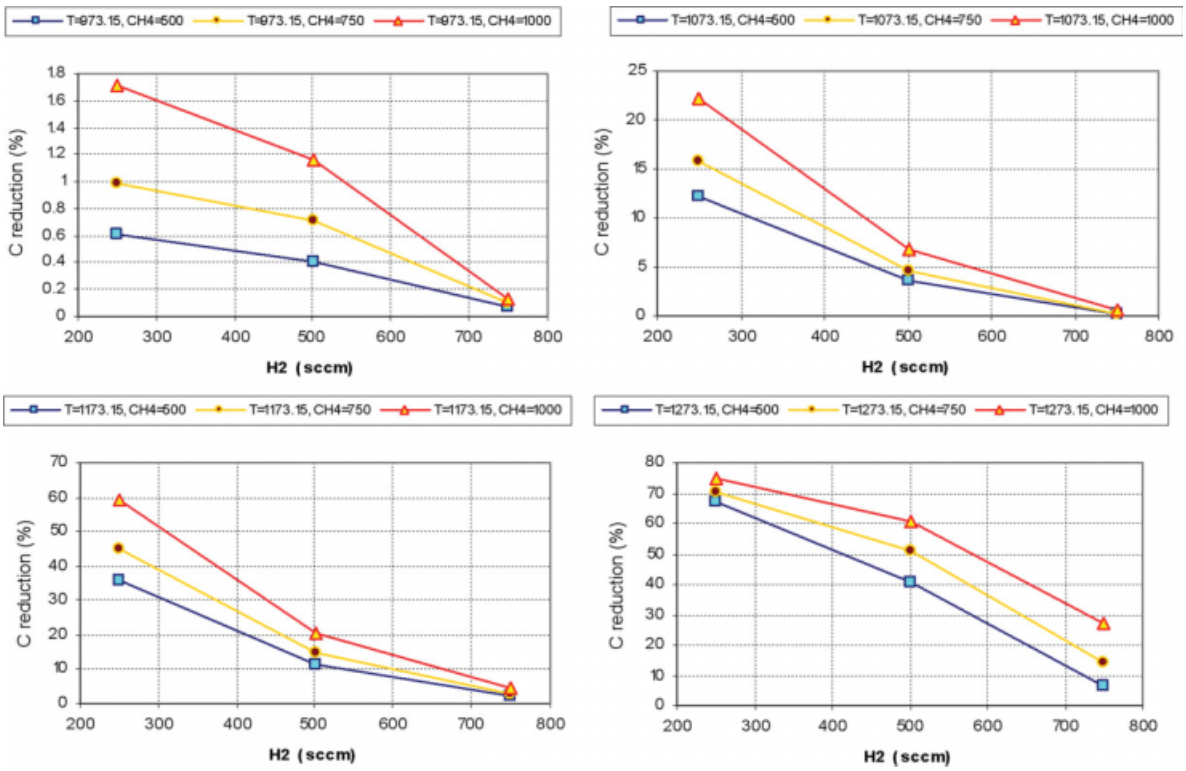

Figure 10. The percentage of carbon decay that participates in CNT construction for different CH_4 + H_2 flow rates (sccm) and temperature (K).

[Color figure can be viewed in the online issue, which is available at www.interscience.wiley.com.]

Although applying H_2 helps minimize the formation of amorphous carbon, as shown earlier in Figures 9 and 10, it also reduces the overall number of available carbon species which are needed to construct CNTs. As a result, the growth rate of CNTs formed near the front edge of the substrate is also studied by considering the total number of available carbon molecules per unit time that are available to participate in CNTs formation. The final results are shown in Figures 11 and 12.

In Figures 11 and 12, it is observed that in most cases increasing the amount of CH_4 flow leads to a higher CNTs growth rate, especially at lower temperatures (973 K), where the amount of the carbon species participating in CNTs or amorphous formation is low. On the other hand, increasing the H_2 flow rate causes the amount of both types of carbon molecules to reduce. However, as the temperature approaches higher values (1073 K), the rate of increase in CNTs growth rate will slow down and more carbon molecules change into amorphous carbon. Because H_2 gas becomes more effective at reducing the percentage of carbon species participating in the production of amorphous carbon as the fabrication temperature increases, a reduction in growth rate of CNTs caused by introducing more H_2 gas into the system will be less tangible when considering the overall CNT growth rate. At 1173 K, the dominant effect of amorphous carbon production on CNTs growth rate results from increasing the flow rate of CH_4 (from 750 sccm to 1000 sccm) at constant (250 sccm) hydrogen flow rate, where these changes lead to a reduction in the CNTs growth rate. However, as more hydrogen gas is inserted into the system, the growth rate of CNTs resembles that seen at lower temperatures (Figure 11). A similar tendency in CNTs growth rate behavior can be observed as the temperature increases to 1273 K, where the growth rate decreases as more CH_4 is inserted into the system.

Therefore, it can be concluded that in order to produce a high yield of clean CNTs at higher fabrication temperatures and for a specific flow rate of CH_4, higher flow rate of H_2 gas is required when compared with that needed for the low temperature CNTs fabrication process. The results of this modeling effort on the amount of amorphous carbon production and the amorphous carbon/CNTs formation ratio for different fabrication temperature and under several hydrocarbon/hydrogen flow rate ratios were compared with the obtained experimental results and showed good agreement (Hosseini et al., submitted). During these experiments, CNTs were fabricated in different temperature and flow rate conditions, and the ratio between amorphous carbon production and CNTs formation on the substrate was investigated by SEM imaging.

The CNTs growth rate is found to vary from less than 0.1 to near 7 micron/s based on the inserted CH_4/H_2 gas ratio and synthesis temperature. Different growth rate numbers have been previously reported by other experimental and theoretical works.[21–27] A comparison of the obtained results with these works shows that the range of CNTs growth rates suggested in this research matches the CNTs growth rate number range found in similar publications. However, a

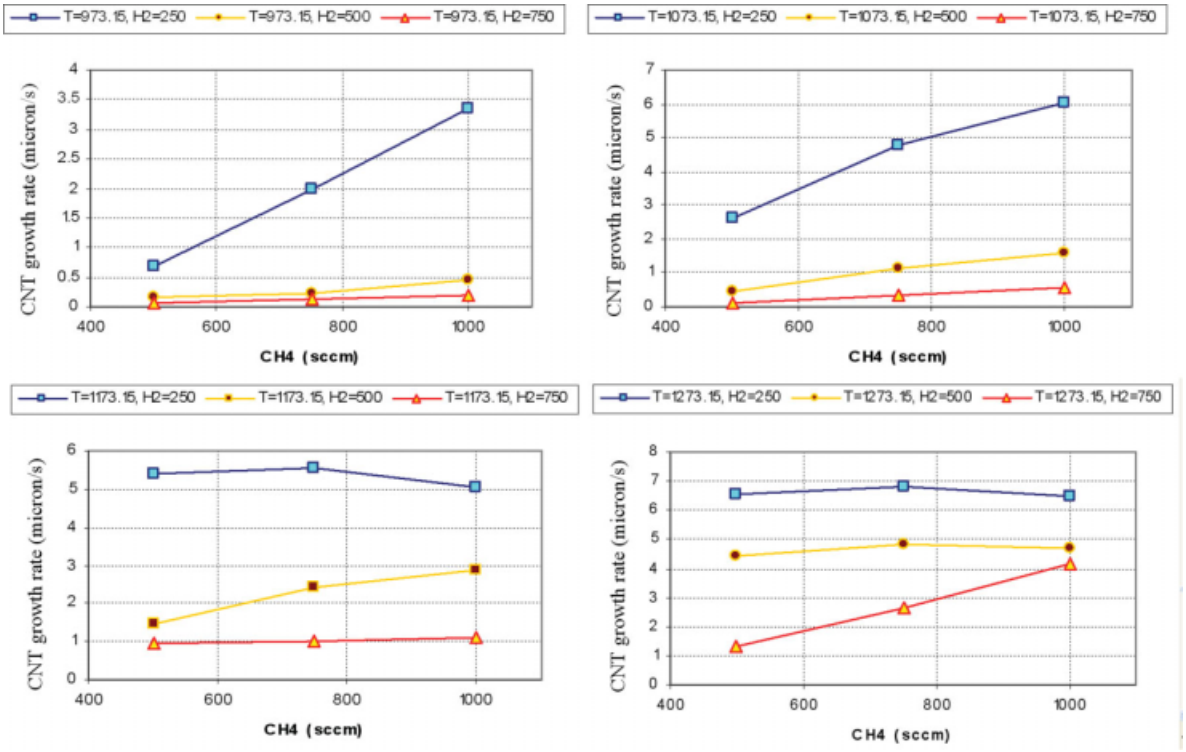

Figure 11. CNT growth rate (micron/s) for different CH_4 + H_2 flow rates (sccm) and temperatures (K).

[Color figure can be viewed in the online issue, which is available at www.interscience.wiley.com.]

direct comparison between the reported experimental data with each other as well as the obtained results from current simulation series is not possible because there is a significant difference between the experimental procedures considered in each study. These experiment-dependent conditions could include, for instance, applied catalyst, nanoparticles'

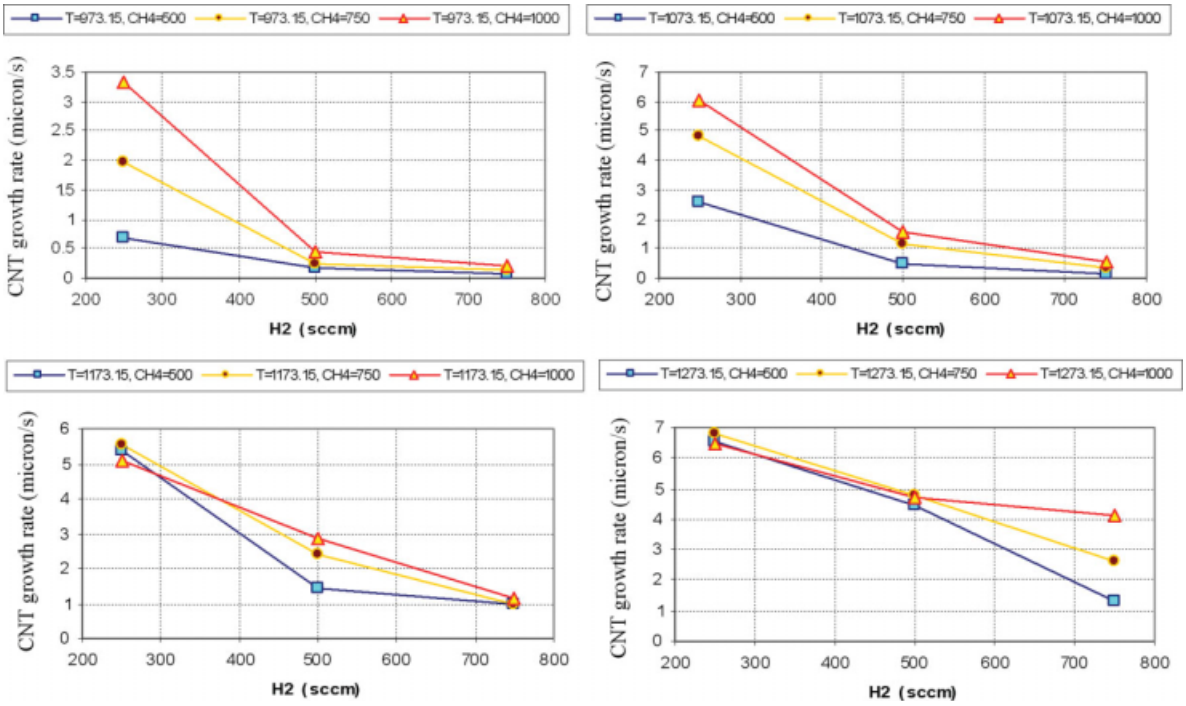

Figure 12. CNT growth rate (micron/s) for different CH_4 + H_2 flow rates (sccm) and temperatures (K).

[Color figure can be viewed in the online issue, which is available at www.interscience.wiley.com.]

deposition methods, geometrical specifications and the reactor type of the fabrication systems, as well as the concentration and the type of gases in the system. Therefore, this theoretical study can provide the vital information that is necessary for a better understanding of how different CNTs fabrication parameters influence final CNTs properties. However, obtaining similar information by experiments is not an easy undertaking due to the need of very expensive setups and many unpredictable and uncontrollable environmental conditions during the procedure which make the final results less reliable. Also, based on our findings, it is possible to explain the reason for discrepancies reported for CNTs growth rate-temperature slope by previous works.[25,27] As mentioned earlier, for most cases, increasing the synthesis temperature causes the CNTs growth rate to increase. However, at high temperatures and for the case where there the H_2 flow rate is low, it can be expected that there would be a decrease in the CNTs growth rate. Therefore, the slope of the CNTs growth rate-temperature curve highly depends on the CH_4/H_2 flow rate ratio.

Conclusions

A time-dependent multiphysics, multiphase-based CVD system model was introduced for a CVD-based CNT fabrication process. CNTs growth rate and the quality of the final product under different synthesis conditions were studied through extensive simulations and experiments. It was observed that increasing CH_4 concentrations will increase the amount of available carbon molecules resulting from gas phase reactions. However, introducing more H_2 into the system will cause a decrease in carbon species, but it increases the concentration of available H molecules. It was concluded that the main role of H_2 gas species during the CNTs fabrication process is to reduce the formation of other undesirable forms of carbon structures, such as amorphous carbon. Because the amount of deposited amorphous carbon increases with temperature, increased H_2 flow is needed to lessen this effect. It was also observed that increases in temperature and CH_4 flow rate increase the CNTs growth rate, except at high fabrication temperatures under insufficient H_2 flow rate, where a reduction in CNTs growth rate occurs. This work can be utilized to optimize CVD-based CNTs fabrication processes, when accompanied by some in-situ measurement or diagnotic systems. Further, these methods allow future optimization efforts to be selectively tuned toward processing cost reductions or CNTs final product criteria.

Acknowledgments

The materials presented here are based upon work supported by the National Science Foundation under CAREER Grant No. CMMI-0238987. Any opinions, findings, and conclusions or recommendations expressed in this material are those of the authors and do not necessarily reflect the views of the National Science Foundation.

Literature Cited

1. Iijima S. Helical microtubules of graphite carbon. *Nature*. 1991; 354:56–58.
2. Tans SJ, Verschueren ARM, Dekker C. Room-temperature transistor based on a single carbon nanotube. *Nature*. 1998;393:49–52.
3. Dai H, Hafner JH, Rinzler AG, Colbert DT, Smalley RE. Nanotubes as nanoprobes in scanning probe microscopy. *Nature*. 1996;384: 147–150.
4. Pancharal P, Wang ZL, Ugarte D, de Heer W. Electrostatic deflections and electromechanical resonances of carbon nanotubes. *Science*. 1999;283:1513–1516.
5. Kong J, Franklin NR, Zhou C, Chapline MG, Peng S, Cho K, Dai H. Nanotube molecular wires as chemical sensors. *Science*. 2000; 287:622–625.
6. Collins PG, Bradley K, Ishigami M, Zettl A. Extreme oxygen sensitivity of electronic properties of carbon nanotubes. *Science*. 2000;287:1801–1804.
7. Dillon AC, Jones KM, Bekkedahl TA, Kiang CH, Bethune DS, Heben MJ. Storage of hydrogen in single-walled carbon nanotubes. *Nature*. 1997;386:377–379.
8. Wang QH, Setlur AA, Lauerhaas JM, Dai JY, Seelig EW, Chang RPH. A nanotube-based field-emission flat panel display. *Appl Phys Lett*. 1998;72:2912–2913.
9. Fan S, Chapline MG, Franklin NR, Tombler TW, Cassell AM, Dai H. Self-oriented regular arrays of carbon nanotubes and their field emission properties. *Science*. 1999;283:512–514.
10. Lee CJ, Kim DW, Lee TJ, Choi YC, Park YS, Kim WS, Lee YH, Choi WB, Lee NS, Kim JM, Choi YG, Yu SC. Synthesis of uniformly distributed carbon nanotubes on a large area of Si substrates by thermal chemical vapor deposition. *Appl Phys Lett*. 1999; 75:1721–1723.
11. Kim P, Lieber CM. Nanotube nanotweezers. *Science*. 1999; 286:2148–2150.
12. Takikawa H, Ikeda M, Hirahara K, Hibi Y, Tao Y, Ruiz Jr PA, Sakakibara T, Itoh S, Iijima S. Fabrication of single-walled carbon nanotubes and nanohorns by means of a torch arc in open air. *Phys B: Condens Matter*. 2001;323:277–279.
13. Scott CD, Arepalli S, Nikolaev P, Smalley RE. Growth mechanisms for single-wall carbon nanotubes in a laser-ablation process. *Appl Phys A: Mater Sci Process*. 2001;72:573–580.
14. Chen C, Chen W, Zhang Y. Synthesis of carbon nano-tubes by pulsed laser ablation at normal pressure in metal nano-sol. *Phys E: Low-Dimensional Syst Nanostruct*. 2005;28:121–127.
15. Li X, Zuo X, Yuan G, Brown A, Westwood A, Brydson R, Rand B. The synthesis of single-walled carbon nanotubes over an Al_2O_3-Fe_2O_3 binary aerogel catalyst. *J Phys: Conf Ser*. 2005;26: 308–311.
16. Clemson University Smart Structures and Nanoelectromechanical Systems (SSNEMS) Laboratory. Available at: www.ces.clemson.edu/ssnems.
17. First Nano Inc. Available at: www.firstnano.com.
18. Li Y, Kim W, Zhang Y, Rolandi M, Wang D, Dai H. Growth of single-walled carbon nanotubes from discrete catalytic nanoparticles of various sizes. *J Phys Chem B*. 2001;105:11424–11431.
19. An L, Owens JM, McNeil LE, Liu J. Synthesis of nearly uniform single-walled carbon nanotubes using identical metal-containing molecular nanoclusters as catalysts. *J Am Chem Soc*. 2002;124: 13688–13689.
20. Siegal MP, Overmyer DL, Provenciopp PP. Precise control of multiwall carbon nanotube diameters using thermal chemical vapor deposition. *Appl Phys Lett*. 2002;80:2171–2173.
21. Klinke C, Kurt R, Bonard JM. Raman spectroscopy and field emission measurements on catalytically grown carbon nanotubes. *J Phys Chem B*. 2002;106:11191–11195.
22. Bonard JM, Chauvin P, Klinke C. Monodisperse multiwall carbon nanotubes obtained with ferritin as catalyst. *Nano Lett*. 2002;2: 665–667.
23. Bonard JM, Croci M, Conus F, Stöckli T, Chatelain A. Watching carbon nanotubes grow. *Appl Phys Lett*. 2002;81:2836–2838.
24. Bonard JM, Croci M, Klinke C, Conus F, Arfaoui I, Stöckli T, Chatelain A. Growth of carbon nanotubes characterized by field emission measurements during chemical vapor deposition. *Phys Rev B*. 2003;67:085412–085423.
25. Geohegan DB, Puretzky AA, Ivanov IN, Jesse S, Eres G, Howe JY. In situ growth rate measurements and length control during chemical vapor deposition of vertically aligned multiwall carbon nanotubes. *Appl Phys Lett*. 2003;83:1851–1853.
26. Lee YT, Park J, Choi YS, Ryu H, Lee HJ. Temperature-dependent growth of vertically aligned carbon nanotubes in the range 800–1100°C. *J Phys Chem B*. 2002;106:7614–7618.

27. Lee CJ, Park J, Huh Y, Lee JY. Temperature effect on the growth of carbon nanotubes using thermal chemical vapor deposition. *Chem Phys Lett*. 2001;343:33–38.
28. Gunjishima I, Inoue T, Okamoto A. In situ optical imaging of carbon nanotube growth. *Jpn J Appl Phys*. 2007;46:3149–3151.
29. Klinke C, Bonard JM, Kern K. Thermodynamic calculations on the catalytic growth of multiwall carbon nanotubes. *Phys Rev B*. 2005;71:035403–035410.
30. Grujicic M, Cao G, Gersten B. Optimization of the chemical vapor deposition process for carbon nanotubes fabrication. *Appl Surf Sci*. 2002;191:223–239.
31. Coltrin ME, Dandy DS. Analysis of diamond growth in subatmospheric dc plasma-gun reactors. *J Appl Phys*. 1993;74:5803–5820.
32. Ruckenstein E, Hu YH. Catalytic preparation of narrow pore size distribution mesoporous carbon. *Carbon*. 1998;36:269–275.
33. Flahaut E, Govindaraj A, Peigney A, Laurent C, Rousset A, Rao CNR. Synthesis of single-walled carbon nanotubes using binary (Fe, Co, Ni) alloy nanoparticles prepared in situ by the reduction of oxide solid solutions. *Chem Phys Lett*. 1999;300:236–242.
34. Westbrook CK, Pitz WJ. A comprehensive chemical kinetic reaction mechanism for oxidation and pyrolysis of propane and propene. *Combust Sci Technol*. 1984;37:117–152.
35. Frenklach M, Wang H. Detailed surface and gas-phase chemical kinetics of diamond deposition. *Phys Rev B*. 1991;43:1520–1545.
36. Dunker AM, Ortmann JP. Kinetic modeling of hydrogen production by thermal decomposition of methane. *Int J Hydrogen Energy*. 2006;31:1989–1998.
37. Neufeld PD, Janzen AR, Aziz RA. Empirical equations to calculate 16 of the transport collision integrals (l,s) for the Lennard-Jones (12-6) potential. *J Chem Phys*. 1972;57:1100–1102.
38. Brokaw RS. Predicting transport properties of dilute gases. *Ind Eng Chem Process Des Dev*. 1969;8:240–253.
39. Stiel LI, Thodos G. The thermal conductivity of nonpolar substances in the dense gaseous and liquid regions. *AIChE J*. 1964;10:26–30.
40. Babushok VI, Tsang W. Kinetic modeling of heptane combustion and PAH formation. *J Propulsion Power*. 2004;20:403–414.
41. Hughes KJ, Turányi T, Clague AR, Pilling MJ. Development and testing of a comprehensive chemical mechanism for the oxidation of methane. *Int J Chem Kinet*. 2001;33:513–538.
42. Orme JP, Curran HJ, Simmie JM. Experimental and modeling study of methyl cyclohexane pyrolysis and oxidation. *J Phys Chem A*. 2006;110:114–131.
43. Smooke MD, Hall RJ, Colket MB, Fielding J, Long MB, McEnally CS, Pfefferle LD. Investigation of the transition from lightly sooting towards heavily sooting co-flow ethylene diffusion flames. *Combust Theory Model*. 2004;8:593–606.
44. Glaude PA, Warth V, Fournet R, Battin-Leclerc R, Scacchi G, Come GM. Modeling of the oxidation of n-octane and n-decane using an automatic generation of mechanisms. *Int J Chem Kinet*. 1998;30:949–959.
45. Egoifopoulos FN, Dimotakis PE. A comparative numerical study of premixed and non-premixed ethylene flames. *Combust Sci Technol*. 2001;162:19–35.
46. Marinov NM. A detailed chemical kinetic model for high temperature ethanol oxidation. *Int J Chem Kinet*. 1999:31;183–220.
47. Fischer SL, Dryer FL, Curran HJ. The reaction kinetics of dimethyl ether. I: high-temperature pyrolysis and oxidation in flow reactors. *Int J Chem Kinet*. 2000;32:713–740.
48. Curran HJ, Pitz WJ, Westbrook CK, Dagaut P, Boettner JC, Cathonnet M. A wide range modeling study of dimethyl ether oxidation. *Int J Chem Kinet*. 1998;30:229–241.
49. Fisher EM, Pitz WJ, Curran HJ, Westbrook CK. Detailed chemical kinetic mechanisms for combustion of oxygenated fuels. *Proc Combust Inst*. 2000;28:1579–1586.
50. Kaiser EW, Wallington TJ, Hurley MD, Plaztz J, Curran HJ, Pitz WJ, Westbrook CK. Experimental and modeling study of premixed atmospheric-pressure dimethyl ether-air flames. *J Phys Chem A*. 2000;104:8194–8206.
51. Glaude PA, Pitz WJ, Thomson MJ. Chemical kinetic modeling of dimethyl carbonate in an opposed-flow diffusion flame. *Proc Combust Inst*. 2005;30:1095–1102.
52. Curran HJ, Gaffuri P, Pitz WJ, Westbrook CK. A comprehensive modeling study of *n*-heptane oxidation. *Combust Flame*. 1998;114:149–177.

Appendix A: Gas Phase and Surface Phase Reactions

Table A1. Gas Phase Reactions

No.	Reaction	A^*	n^*	E^*	References/comments
	CH_4 reactions				
G1	$CH_4 + H \leftrightarrow CH_3 + H_2$	6.60×10^8	1.62	45,357	40
G2	$CH_4 + CH \leftrightarrow C_2H_4 + H$	6.0×10^{13}	0.0	0.0	31
G3	$CH_4 + C \leftrightarrow CH + CH_3$	5×10^{13}	0.0	100,480	41
G4	$CH_4 + C_2H \leftrightarrow C_2H_2 + CH_3$	1.81×10^{12}	0.0	2092	42
G5	$CH_4 + CH_2 \leftrightarrow CH_3 + CH_3$	2.46×10^6	2.0	34,603	43
G6	$CH_4 + M \leftrightarrow CH_3 + M + H$	2.4×10^{16}	0.0	437,249	44
	CH_3 reactions				
G7	$CH_3 + CH_3 + M \leftrightarrow C_2H_6 + M$	9.03×10^{16}	−1.18	2736.336	$31/H_2$ enhancement = 2.0
G8	$CH_3 + H + M \leftrightarrow CH_4 + M$	6.0×10^{16}	−1.0	0.0	$31/H_2$ enhancement = 2.0
G9	$CH_3 + H \leftrightarrow CH_2 + H_2$	9.0×10^{13}	0.0	63,178.4	31
G10	$CH_3 + CH \leftrightarrow C_2H_3 + H$	3.0×10^{13}	0.0	0.0	31
G11	$CH_3 + C \leftrightarrow C_2H_2 + H$	5.0×10^{13}	0.0	0.0	31
G12	$CH_3 + C_2H_6 \leftrightarrow C_2H_5 + CH_4$	5.5×10^{-1}	4.0	34,727.2	31
G13	$CH_3 + CH_3 \leftrightarrow C_2H_5 + H$	4.99×10^{12}	0.1	44,352	45
G14	$CH_3 + H_2 \leftrightarrow CH_4 + H$	4.13×10^4	2.50	39.4	35
G15	$CH_3 + M \leftrightarrow CH_2 + H + M$	2.90×10^{16}	0.0	379	$35/M = H_2$
G16	$CH_3 + CH_2 \leftrightarrow C_2H_4 + H$	3×10^{13}	0.0	0.0	31
G17	$CH_3 + C_2H_4 \leftrightarrow C_2H_3 + CH_4$	4.20×10^{11}	46.5	35	35
G18	$CH_3 + C_2H_2 \leftrightarrow C_2H + CH_4$	1.81×10^{11}	0.0	72,341	46
G19	$CH_3 + C_2H_3 \leftrightarrow C_2H_2 + CH_4$	3.92×10^{11}	0.0	0.0	42
G20	$CH_3 + C_2H_5 \leftrightarrow C_2H_4 + CH_4$	1.95×10^{13}	−0.50	0.0	47
	CH_2 reactions				
G21	$CH_2 + H \leftrightarrow CH + H_2$	1.0×10^{18}	−1.56	0.0	31
G22	$CH_2 + CH \leftrightarrow C_2H_2 + H$	4.0×10^{13}	0.0	0.0	31
G23	$CH_2 + C \leftrightarrow C_2H + H$	5.0×10^{13}	0.0	0.0	31
G24	$CH_2 + C_2H_3 \leftrightarrow C_2H_2 + CH_3$	3.0×10^{13}	0.0	0.0	31
G25	$CH_2 + CH_2 \leftrightarrow C_2H_2 + H_2$	4.0×10^{13}	0.0	0.0	31

Table A1. (*Continued*)

No.	Reaction	A^*	n^*	E^*	References/comments
G26	$CH_2 + H_2 \leftrightarrow CH_3 + H$	7.23×10^{13}	0.0	0.0	35
G27	$CH_2 + C_2H \leftrightarrow C_2H_2 + CH$	1.8×10^{13}	0.0	0.0	44
G28	$CH_2 + C_2H_5 \leftrightarrow C_2H_4 + CH_3$	1.80×10^{13}	0.0	0.0	44
G29	$CH_2 + C_2H_6 \leftrightarrow C_2H_5 + CH_3$	2.20×10^{13}	0.0	36,277	48
	CH reactions				
G30	$CH + H \leftrightarrow C + H_2$	1.5×10^{14}	0.0	0.0	31
G31	$CH + H_2 \leftrightarrow CH_2 + H$	1.08×10^{14}	0.0	13,013	40
G32	$CH + M + H_2 \leftrightarrow CH_3 + M$	1.97×10^{12}	0.43	−1548	40
G33	$CH+C_2H_6 \leftrightarrow C_2H_5+CH_2$	1.10×10^{14}	0.0	−1088	49
G34	$CH + C_2H_2 \leftrightarrow C_2H + CH_2$	2.11×10^{14}	0.0	−510	41
	C reactions				
G35	$C + H_2 \leftrightarrow CH + H$	4×10^{14}	0.0	97,492	44
	C_2H reactions				
G36	$C_2H + H_2 \leftrightarrow C_2H_2 + H$	4.09×10^{5}	2.39	3616.2312	31
G37	$C_2H + C_2H_3 \leftrightarrow C_2H_2 + C_2H_2$	3.0×10^{13}	0.0	0.0	31
G38	$C_2H + C_2H_5 \leftrightarrow C_2H_2 + C_2H_4$	1.8×10^{12}	0.0	0.0	44
G39	$C_2H + C_2H_6 \leftrightarrow C_2H_2 + C_2H_5$	3.6×10^{12}	0.0	0.0	44
	C_2H_2 reactions				
G40	$C_2H_2 + C_2H_4 \leftrightarrow C_2H_3 + C_2H_3$	2.41×10^{13}	0.0	286,032	40
G41	$C_2H_2 + M \leftrightarrow C_2H + H + M$	4.2×10^{16}	0.0	447,688	31
G42	$C_2H_2 + H + M \leftrightarrow C_2H_3 + M$	5.6×10^{12}	0.0	10,042	31
	C_2H_3 relations				
G43	$C_2H_3 + H \leftrightarrow C_2H_2 + H_2$	4.0×10^{13}	0.0	0.0	31
G44	$C_2H_3 + CH \leftrightarrow CH_2 + C_2H_2$	5.0×10^{13}	0.0	0.0	31
G45	$C_2H_3 + C_2H_3 \leftrightarrow C_2H_2 + C_2H_4$	9.6×10^{11}	0.0	0.0	42
G46	$C_2H_3 + C_2H_5 \leftrightarrow C_2H_4 + C_2H_4$	3.0×10^{12}	0.0	0.0	50
G47	$C_2H_3 + C_2H_6 \leftrightarrow C_2H_4+C_2H_5$	6.0×10^{2}	3.30	43,934	44
	C_2H_4 reactions				
G48	$C_2H_4 + H \leftrightarrow C_2H_3 + H_2$	1.1×10^{14}	0.0	35,564	31
G49	$C_2H_4 + M \leftrightarrow C_2H_2 + H_2 + M$	1.5×10^{15}	0.0	233,467.2	31
G50	$C_2H_4 + M \leftrightarrow C_2H_3 + H + M$	1.4×10^{16}	0.0	344,594.24	31
G51	$C_2H_4 + H_2 \leftrightarrow CH_3 + CH_3$	3.77×10^{12}	0.83	354,443	51
G52	$C_2H_4 + C_2H_4 \leftrightarrow C_2H_3 + C_2H_5$	4.82×10^{14}	0.0	299,333	40
G53	$C_2H_4 + C_2H_6 \leftrightarrow C_2H_5 + C_2H_5$	5.0×10^{11}	0.0	251,052	52
G54	$C_2 H_4 + H + M \leftrightarrow C_2H_5 + M$	2.21×10^{13}	0.0	8644.144	31/H_2 enhancement = 2.0
	C_2H_5 reactions				
G55	$C_2H_5 + H \leftrightarrow CH_3 + CH_3$	1.0×10^{14}	0.0	0.0	31
G56	$C_2H_5 + C_2H_5 \leftrightarrow C_2H_4+C_2H_6$	1.4×10^{12}	0.0	0.0	44
	C_2H_6 reaction				
G57	$C_2H_6 + H \leftrightarrow C_2H_5 + H_2$	5.4×10^{2}	3.5	21,798.64	31
	H and H_2 reactions				
G58	$H + H + M \leftrightarrow H_2 + M$	1.0×10^{18}	−1.0	0.0	31/H_2 enhancement = 0
G59	$H + H + H_2 \leftrightarrow H_2 + H_2$	9.2×10^{16}	−0.6	0.0	31
G60	$H_2 + M \leftrightarrow M + H + H$	4.57×10^{19}	−1.40	436,830	42

*The unit for A is given in terms of mol, cm^3 and s and for E as joule/mol; n is unitless.

Table A2. Surface Phase Reactions Accompanying CNT Formation[30]

No.	Reaction	A^*	n^*	E^*
SNT1	$T(S) + H \leftrightarrow TH(S)$	1.0×10^{13}	0.0	0.0
SNT2	$T(S) + CH_3 \leftrightarrow TCH_3(S)$	5.0×10^{12}	0.0	0.0
SNT3	$T(S) + C_2H_2 \leftrightarrow TC_2H_2(S)$	8.0×10^{10}	0.0	32.2168
SNT4	$TH(S) + H \leftrightarrow T(S) + H_2$	1.3×10^{14}	0.0	30.5432
SNT5	$TCH_3(S) + H \leftrightarrow TCH_2(S,R) + H_2$	2.8×10^{7}	2.0	32,216.8
SNT6	$TCH_2(S,R) + H \leftrightarrow TCH_3(S)$	1.0×10^{13}	0.0	0.0
SNT7	$TCH_2(S,R) + H \leftrightarrow TCH(S,R_2) + H_2$	2.8×10^{7}	2.0	32,216.8
SNT8	$TCH(S,R_2) + H \leftrightarrow TCH_2(S,R)$	1.0×10^{13}	0.0	0.0
SNT9	$TCH_2(S,R) + H \leftrightarrow T(S) + CH_3$	3.0×10^{13}	0.0	0.0
SNT10	$TCH(S,R_2) + H \leftrightarrow TC(S,R_3) + H_2$	2.8×10^{7}	2.0	32,216.8
SNT11	$TC(S,R_3) + H \leftrightarrow TCH(S,R_2)$	1.0×10^{13}	0.0	0.0
SNT12	$TCH(S,R_2) + CH_3 \leftrightarrow TCHCH_3(S,R)$	5.0×10^{12}	0.0	0.0
SNT13	$TCH_2(S,R) + CH_3 \leftrightarrow TCH_2CH_3(S)$	5.0×10^{12}	0.0	0.0
SNT14	$TCH_2CH_3(S) + H \leftrightarrow TCHCH_3(S,R) + H_2$	9.0×10^{6}	2.0	20,920

Table A2. (*Continued*)

No.	Reaction	A^*	n^*	E^*
SNT15	$TCHCH_3(S,R) + H \leftrightarrow TCH_2CH_3(S)$	2.0×10^{13}	0.0	0.0
SNT16	$TCHCH_3(S,R) + H \leftrightarrow TCCH_3(S,R_2) + H_2$	9.0×10^{6}	2.0	20,920
SNT17	$TCCH_3(S,R_2) + H \leftrightarrow TCHCH_3(S,R)$	2.0×10^{13}	0.0	0.0
SNT18	$TC_2H_y(S,R_{2-y}) + H \leftrightarrow TC_2H_{y-1}(S,R_{3-y}) + H_2$[†]	9.0×10^{6}	2.0	20,920
SNT19	$TC_y(S,R_{2-y}) \leftrightarrow T(S) + yC(B)$			

*The unit for A is given in terms of mol, cm^3 and s and for E as joule/mol; n is unitless.
[†]$y = 1,2$.

Table A3. Surface Phase Reactions Accompanying Amorphous Carbon Formation[30]

No.	Reaction	A^*	E^*	Comments
SAC1	$C(S,R) + H \leftrightarrow CH(S)$	0.03	0.0	b
SAC2	$C(S,R) + CH3 \leftrightarrow CH3(S) + C(A)$	0.033	0.0	b
SAC3	$C(S,R) + C_2H_2 \leftrightarrow C_2H_2(S,R) + H_2$	0.033	0.0	b
SAC4	$CH(S) + H \leftrightarrow C(S,R) + H_2$	0.0214	30,543.2	b
SAC5	$CH_2(S,R) + H \leftrightarrow CH_3(S)$	0.3	0.0	b
SAC6	$CH_3(S) + H \leftrightarrow CH_2(S,R) + H_2$	4.28	30,543.2	b
SAC7	$CH(S,R_2) + H \leftrightarrow CH_2(S,R)$	0.3	0.0	b
SAC8	$CH(S,R_2) + H_2 \leftrightarrow CH_3(S)$	0.3	0.0	b
SAC9	$C(S,R_3) + H \leftrightarrow CH(S,R_2)$	0.3	0.0	b
SAC10	$C(S,R_3) + H_2 \leftrightarrow CH_2(S,R_2)$	0.3	0.0	b
SAC11	$CH_2(S) + H \leftrightarrow CH(S,R) + H_2$	2.14	30,543.2	b
SAC12	$CH(S,R) + H \leftrightarrow CH_2(S)$	0.3	0.0	b
SAC13	$CH_2(S,R) + CH(S,R) \leftrightarrow CH_2(S) + CH(S)$	6.0×10^{19}	0.0	a
SAC14	$CH(S) + C_2H_2(S,R) \leftrightarrow C(S,R) + C_2H_3(S)$	6.0×10^{19}	0.0	a
SAC15	$C(S,R_3) + CH_2(S) \leftrightarrow CH(S,R) + CH(S)$	6.0×10^{19}	0.0	a

*The unit for A is given in terms of mol, cm^3 and s and for E as joule/mol, with $n = 0$ in Eq. (3).

Manuscript received Nov. 12, 2008, and revision received Apr. 22, 2009.